IEEE Access
Multidisciplinary | Rapid Review | Open Access Journal

Received 27 December 2023, accepted 5 January 2024, date of publication 8 January 2024,
date of current version 19 January 2024.

Digital Object Identifier 10.1109/ACCESS.2024.3351509

RESEARCH ARTICLE

Robust Model-Free Fault-Tolerant Predictive Control for PMSM Drive System

SHU CHENG[1], RUIRUI ZHOU[1], (Graduate Student Member, IEEE), ZHUOXIN LI[1], ZHEN XI[1], JUNDONG ZHAO[1], KAIHUI ZHAO[2], (Senior Member, IEEE), AND CHAOQUN XIANG[1], (Member, IEEE)

[1]School of Traffic and Transportation Engineering, Central South University, Changsha 410075, China
[2]School of Electrical and Information Engineering, Hunan University of Technology, Zhuzhou 412007, China

Corresponding author: Chaoqun Xiang (xiangchq@csu.edu.cn)

This work was supported in part by the National Key Research and Development Project of China under Grant 2022YFB4201602-02, in part by the National Natural Science Foundation of China under Grant 52072414, in part by the Postgraduate Scientific Research Innovation Project of Hunan Province of China under Grant QL20230073, and in part by the Postgraduate Innovative Project of Central South University under Grant 2022XQLH195.

ABSTRACT The parameter mismatch caused by the parameter uncertainties and unknown disturbances degrades the performance of finite-control-set model predictive control (FCS-MPC). This paper presents a model-free fault-tolerant predictive control (MFFTPC) method based on an extended sliding mode observer (ESMO) for the surface-mounted permanent magnet synchronous motor (SPMSM) drive system. First, considering parameter uncertainties and unknown disturbances, a novel ultra-local model (ULM) is established for the PMSM drive system. Next, a finite-control-set model-free fault-tolerant predictive current controller (FCS-MFFTPCC) is designed in the current loop, and the model-free deadbeat fault-tolerant predictive speed controller (MFDFTPSC) is designed in the speed loop. Then, unknown parts of the novel ULM are estimated by the designed ESMO and compensated for the errors caused by the parameter mismatches. Thus, the presented method reduces the dependence on the precise model and eliminates the effect caused by parameter mismatches on the MPC control performance of the SPMSM drive system.

INDEX TERMS Surface-mounted permanent magnet synchronous motor (SPMSM), ultra-local model (ULM), model-free fault-tolerant predictive control, parameter mismatches, extended sliding mode observer (ESMO).

I. INTRODUCTION

Permanent magnet synchronous motor (PMSM) has been widely employed in industrial applications, e.g. electric vehicles and rail transit, owing to its excellent dynamic characteristics [1]. In a PMSM drive system, the conventional proportional-integral (PI) controllers are extensively applied because of their easy implementation. However, the performance of the PI controller is limited for high-performance drive systems due to the integral windup [2].

In high-precision and high-performance engineering applications, the PMSM drive system requires fast torque response and small fluctuations [3]. The predictive control method [4] has some features for fast dynamic response and easy multi-objective collaboration [5]. Therefore, it has been developed and widely used in industrial drives. Generally speaking, predictive control can be categorized into two groups: deadbeat predictive control (DPC) and model predictive control (MPC). MPC can be divided into the continuous control set MPC (CCS-MPC) and the finite control set MPC (FCS-MPC). FCS-MPC is a popular research topic that corresponds with power electronic converters with discrete switching states [6]. It evaluates each candidate state by cost function and output the optimal state to control the inverter [7].

However, FCS-MPC relies heavily on the precise mathematical model of the motor. The control performance of the FCS-MPC method is easily affected by the parameter

The associate editor coordinating the review of this manuscript and approving it for publication was Alfeu J. Sguarezi Filho.

perturbations [8], such as stator inductance variation, stator resistance variation, and permanent magnet (PM) demagnetization faults [9]. In practical engineering applications, the resistance and inductance are affected by temperature and the operating conditions [10] the PM material of the rotor is affected by temperature, an external magnetic field, manufacturing defects, and so on [11], thus resulting in the demagnetization fault. The PM flux will reduce 20% of the initial flux per $100°C$ increase in the ambient temperature [12]. The parameter perturbation brings about the parameter mismatches of the FCS-MPC [13], which greatly affects the performance of PMSM drive systems [14].

To retain the advantages of predictive control while solving the shortcomings of parameter sensitivity, some researchers have improved parameter-identification-based methods [15], [16], [17]. This kind of method aims to correct controller parameters by identifying motor parameters in real-time. However, unmodeled non-linear factors, such as inverter dead-time [15], cross-coupling of magnetic circuits [18], will directly affect the accuracy of the identification results. Meanwhile, complex identification algorithms will also increase the calculation burden of predictive control [19].

The PM demagnetization fault diagnosis is the basis for executing fault-tolerant operation of PMSM drive systems. A data-driven diagnosis method based on motor electromagnetic or mechanical signature analysis obtains demagnetization fault information by using wavelet packet transform [20], custom phase space reconstruction image [21], and dynamic Bayesian network [22]. To avoid the selection of preset parameters, the Ramanujan digital twin architecture is used to detect the potential fault signatures [23]. However, these methods are difficult to directly connect with the fault-tolerant control, and requires a large amount of computation. The model-based approach constructs an online observer for PM flux linkage by dynamic data processing techniques. This method can provide quantitative data for demagnetization fault diagnosis and is easy to integrate with other schemes to perform fault-tolerant control. A sliding mode-based flux linkage observer is applied to diagnose the demagnetization fault [24].

The model-free control (MFC) [25] proposed by Fliess and Join provides a new solution for fault-tolerant control of parameter perturbations in the PMSM. Compared with model-based control strategies, the MFC methods can reduce the dependence of the controller on the system model, and significantly improve the motor control performance. The input and output information of the motor are used to construct an ultra-local model (ULM), and then an ULM-based MFC controller is designed. To achieve a better demagnetization fault-tolerant control performance, the feedback controller in MFC was designed as a nonsingular terminal sliding mode controller (SMC) [26] and super-twisting SMC [27]. A model-free adaptive internal terminal SMC with a nonlinear disturbance observer was presented for a PMSM drive system [28]. The model-free deadbeat predictive current control was implemented by applying the

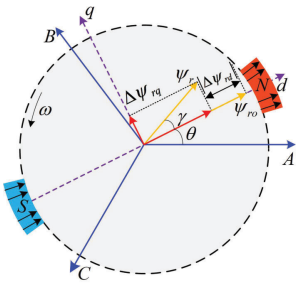

FIGURE 1. The variation of PM flux in PMSM.

ULM of a surface-mounted PMSM (SPMSM) [29]. Although this method has some effects on performance enhancement, the influence of motor parameter perturbations was not considered.

This paper presents an MFFTPC method based on ESMO (called ESMO-based MFFTPC hereafter) to perform fault-tolerant control for the SPMSM drive systems. It aims to enhance the robustness and eliminate the effect of parameter perturbations on predictive control. The main contributions of this study are as follows:

i) By combining MFC and MPC, an MFFTPC strategy is introduced to achieve fault-tolerant control for SPMSM with parameter perturbation. The MFFTPC strategy involves the double advantages of MPC and MFC. That is, it can not only maintain the independence of an accurate SPMSM model but also obtain higher robustness and strong stability of SPMSM.

ii) An FCS-MFFTPCC method is designed based on the novel ULM in the current loop, and an MFDFTPSC method is designed based on the novel ULM in the speed loop, respectively. That greatly enhances the response speed of the SPMSM drive system with parameter perturbation.

iii) The unknown parts of the novel ULM are accurately estimated by the designed ESMO for the first time, so that the predictive model is consistent with the actual motor model. Unlike the conventional current-based cost function, a voltage-based cost function is presented to obtain the optimal voltage vector through only calculation and comparison once.

The rest of this paper is organized as follows. Section II introduces the novel ULM of SPMSM with parameter perturbations. Section III presents the MFFTPC method. Section IV explains the configuration of the ESMO. Section V and VI give the simulation and experimental results to validate the effectiveness of the proposed MFFTPC method. Section VII gives the conclusion.

II. SYSTEM DESCRIPTION

This section describes a novel ULM of SPMSM with parameter perturbations in the d-q reference frame.

A. MATHEMATICAL MODEL OF PMSM WITH PARAMETER PERTURBATIONS

When PM demagnetization fault occurs [30], the amplitude of PM flux changes from ψ_{ro} to ψ_r, and/or the direction of

PM flux varies from 0 to γ (see Figure 1). The variations of rotor flux are $\Delta\psi_{rd} = \psi_{ro}\cos\gamma - \psi_{ro}$, $\Delta\psi_{rq} = \psi_{ro}\sin\gamma$.

Considering the motor parameter perturbations, such as resistance variation, inductance variation [31], PM demagnetization fault, the state equation of SPMSM in the d-q reference frame is expressed as

$$\begin{cases} \dfrac{di_d}{dt} &= -\dfrac{R_{so}}{L_{so}}i_d + \dfrac{1}{L_{so}}u_d + \omega_e i_q + \delta_d \\ \dfrac{di_q}{dt} &= -\dfrac{R_{so}}{L_{so}}i_q + \dfrac{1}{L_{so}}u_q - \omega_e i_d - \dfrac{\omega_e}{L_{so}}\psi_{ro} + \delta_q \end{cases} \tag{1}$$

where

i_d, i_q: d- and q-axes stator current (A);
u_d, u_q: d- and q-axes stator voltage (V);
L_{so}: nominal stator inductance (H);
R_{so}: nominal stator resistance (Ω);
ψ_{ro}: nominal amplitude of PM flux (Wb);
ω_e: electrical angular velocity (rad/s);
δ_d, δ_q:unknown disturbances.

$$\begin{cases} \delta_d = -\dfrac{\Delta L_s}{L_{so}\left(L_{so}+\Delta L_s\right)}\left(u_d - R_{so}i_d - \Delta R_s i_d + L_{so}\omega_e i_q \right. \\ \left. +\Delta L_s\omega_e i_q + \omega_e\Delta\psi_{rq}\right) - \dfrac{1}{L_{so}}\left(\Delta R_s i_d - \Delta L_s\omega_e i_q - \omega_e\Delta\psi_{rq}\right) \\ \delta_q = -\dfrac{\Delta L_s}{L_{so}\left(L_{so}+\Delta L_s\right)}\left(u_q - R_{so}i_q - \Delta R_s i_q - L_{so}\omega_e i_d \right. \\ \left. -\Delta L_s\omega_e i_d - \omega_e\psi_{ro} - \omega_e\Delta\psi_{rd}\right) - \dfrac{1}{L_{so}}\left(\Delta R_s i_q + \Delta L_s\omega_e i_d \right. \\ \left. +\omega_e\Delta\psi_{rd}\right). \end{cases}$$

where $\Delta R_s = R_s - R_{so}$ is the variation of stator resistance and $\Delta L_s = L_s - L_{so}$ the variation of stator inductances, R_s and L_s are actual stator resistance and stator inductances, respectively.

Considering parameter uncertainties and unknown disturbances, the mechanical equation of an SPMSM is expressed as

$$\frac{d\omega_e}{dt} = -\frac{B}{J}\omega_e + \frac{3}{2}\frac{n_p^2}{J}\psi_{ro}i_q + \frac{n_p}{J}(-T_L + \Delta T_e + \Delta T_L + \varepsilon) \tag{2}$$

where n_p is the number of pole pairs; J and B are rotational inertia and viscous friction coefficient, respectively; $\Delta T_e = \frac{3}{2}n_p\Delta\psi_{rd}i_q$, ΔT_e is the perturbation of electromagnetic torque; ΔT_L is the disturbance of the load torque; ε indicates other unknown disturbances.

B. NOVEL ULM OF SPMSM WITH PARAMETER PERTURBATIONS

1) THE CONVENTIONAL ULM

For a single-input single-output nonlinear system, the ULM is expressed as [25]

$$\begin{cases} \dot{x} &= f(x) + \beta u \\ y &= x \end{cases} \tag{3}$$

where x, y, and u are the state variable, the system output, and the control input, respectively; f is the unknown Lipschitz bounded nonlinear function depending only on x, including the bounded disturbance; β is a priori-known constant, which is chosen to keep βu and $\dot{x}$ in the same order.

2) THE NOVEL ULM

The nonlinear component, $f(x)$, is expressed as [32]

$$f(x) = \alpha x + h \tag{4}$$

where α is the gain of system state; h is the unknown nonlinear part, which satisfies Lipschitz bounded with Lebesgue measurability.

According to (4), the nonlinear component, f, is further divided into the linear part and nonlinear part. Therefore, the novel ULM of system (3) can be expressed as follows

$$\begin{cases} \dot{x} &= \alpha x + \beta u + h \\ y &= x. \end{cases} \tag{5}$$

According to (1), (2), and (5), the novel ULMs of SPMSM in the speed loop and d-q-axis current loops are designed as

$$\dot{\boldsymbol{x}} = \boldsymbol{\alpha x} + \boldsymbol{\beta u} + \boldsymbol{h} \tag{6}$$

where $\boldsymbol{x} = \begin{bmatrix} i_d & i_q & \omega_e \end{bmatrix}^T$ is the state variables; $\boldsymbol{u} = \begin{bmatrix} u_d & u_q & i_q \end{bmatrix}^T$ is the control input; $\boldsymbol{\alpha} = diag\left(\alpha_d, \alpha_q, \alpha_\omega\right)$, α_d, α_q are the designed current gains, and α_ω is the designed speed gain; $\boldsymbol{\beta} = diag\left(\beta_d, \beta_q, \beta_\omega\right)$, β_d, β_q are the designed voltage parameters, and β_ω is the designed current parameter; $\boldsymbol{h} = \begin{bmatrix} h_d & h_q & h_\omega \end{bmatrix}^T$ are the unknown parts, including the modeled part and the disturbance part of SPMSM, which satisfy the Lipschitz bounded condition.

Remark 1. *Note that, although $\boldsymbol{\alpha}$ and $\boldsymbol{\beta}$ are pre-designed coefficient matrices, even if they are not very accurate, the control performance of the SPMSM drive system is maintained by adjusting $\boldsymbol{h}$. Thus, precise parameters are not required, which is one of the advantages of MFC based on the ULM [33].*

III. DESIGN OF MFFTPC

Based on the novel ULM, an FCS-MFFTPCC in the d-q-axis current loops, and a MFDFTPSC in the speed loop are designed, respectively.

A. DESIGN OF FCS-MFFTPCC IN D-Q-AXIS CURRENT LOOPS

The discrete novel ULM in the d-q-axis current loops is derived from (6) by using the first-order forward-Euler method

$$\boldsymbol{i}^p(k+1) = \left[\boldsymbol{\alpha}_{dq}\boldsymbol{i}(k) + \boldsymbol{\beta}_{dq}\boldsymbol{u}_{dq}(k) + \boldsymbol{h}_{dq}(k)\right]T_{sc} + \boldsymbol{i}(k) \tag{7}$$

where $\boldsymbol{i}^p(k+1) = \begin{bmatrix} i_d^p(k+1) & i_q^p(k+1) \end{bmatrix}^T$ indicates the current predictive values at $(k+1)T_{sc}$ instant; $\boldsymbol{i}(k) = \begin{bmatrix} i_d(k) & i_q(k) \end{bmatrix}^T$ represents the current measured values at kT_{sc} instant; $\boldsymbol{u}_{dq}(k) = \begin{bmatrix} u_d(k) & u_q(k) \end{bmatrix}^T$ is the chosen voltage vector at kT_{sc} instant; $\boldsymbol{\alpha}_{dq} = diag\left(\alpha_d, \alpha_q\right)$;

$\boldsymbol{\beta}_{dq} = diag\left(\beta_d, \beta_q\right)$; $\boldsymbol{h}_{dq}(k) = \left[h_d(k) \quad h_q(k)\right]^T$ is the uncertain part caused by the perturbation of motor parameters and the nonlinearity of inverter, they are updated at every sampling period; T_{sc} is the sampling time of the current loop.

The control goal is to keep the actual current close to the reference current, and the cost function is defined as

$$g = \left[i_d^* - i_d^p(k+1)\right]^2 + \left[i_q^* - i_q^p(k+1)\right]^2 \tag{8}$$

where i_d^* and i_q^* are the current references.

The computational burden increases when using (7) and (8) to obtain indirectly the optimal voltage vector. So, it is necessary to convert the optimization objective. The control goal of the FCS-MFFTPCC is to make the current predictive values accurately tracking the references i_d^* and i_q^*, namely, $i_d^p(k+1) = i_d^*$, $i_q^p(k+1) = i_q^*$. Then, the reference voltage predictive model is obtained

$$\boldsymbol{u}^* = \boldsymbol{\beta}_{dq}^{-1}\left[\frac{1}{T_{sc}}\boldsymbol{i}^* - \left(\boldsymbol{\alpha}_{dq} + \frac{\boldsymbol{I}}{T_{sc}}\right)\boldsymbol{i}(k) - \boldsymbol{h}_{dq}(k)\right] \tag{9}$$

where $\boldsymbol{u}^* = \left[u_d^* \; u_q^*\right]^T$ are d- and q-axes the predictive reference voltage; $\boldsymbol{i}^* = \left[i_d^* \; i_q^*\right]^T$; $\boldsymbol{I}$ is the identity matrix.

Converting the cost function based on current into the cost function based on voltage, the corresponding cost function is rewritten as

$$g = \left(u_d^* - u_d\right)^2 + \left(u_q^* - u_q\right)^2 \tag{10}$$

Remark 2. *The predicted reference voltage is calculated by (9) and substituted into (10) to select the optimal voltage vector, $\boldsymbol{u}_{opt}$. The selected $\boldsymbol{u}_{opt}$ which is equivalent to the conventional predictive current method. But it is not necessary to predict the current seven times according to (7), only calculate (9) once to obtain $\boldsymbol{u}_{opt}$.*

The delay compensation method of ''two-step calculation'' is used to solve the problem of ''one-step delay'' [34].

B. DESIGN OF MFDFTPSC IN SPEED LOOP

The discrete novel ULM in the speed loop is obtained from (6)

$$\omega_e(k+1) = \left(h_\omega(k) + \alpha_\omega\omega_e(k) + \beta_\omega i_q(k)\right)T_{ss} + \omega_e(k) \tag{11}$$

where T_{ss} is the sampling period of the speed loop.

The q-axis reference current is predictively obtained by the discrete ULM (11), and the speed tracks the reference speed during the next control period. The reference speed $\omega_e^*(k+1)$ is considered as $\omega_e(k+1)$ at $(k+1)T_{ss}$ instant. Therefore, the q-axis reference current is described as

$$i_q^*(k) = \frac{\omega_e^*(k+1) - \omega_e(k) - h_\omega(k)T_{ss} - \alpha_\omega\omega_e(k)T_{ss}}{\beta_\omega T_{ss}} \tag{12}$$

IV. DESIGN OF ESMO TO ESTIMATE UNKNOWN PARTS

This section designs the ESMO to estimate the unknown parts $\boldsymbol{h}$ in the novel ULM.

A. DESIGN OF ESMO

To accurately estimate unknown parts $\boldsymbol{h}$, that is $\boldsymbol{h}_{dq}$ in (9) and h_ω in (12), the extended novel ULM of SPMSM is obtained from (6)

$$\begin{cases} \dot{\boldsymbol{x}} &= \boldsymbol{\alpha}\boldsymbol{x} + \boldsymbol{\beta}\boldsymbol{u} + \boldsymbol{h} \\ \dot{\boldsymbol{h}} &= \boldsymbol{H} \end{cases} \tag{13}$$

where $\boldsymbol{H} = \left[H_d \; H_q \; H_\omega\right]^T$ are the variation rates of unknown parts $\boldsymbol{h} = \left[h_d \quad h_q \quad h_\omega\right]^T$, and they are regarded as constant in engineering.

To accurately estimate the unknown parts, the ESMO is designed as

$$\begin{cases} \dot{\hat{\boldsymbol{x}}} &= \boldsymbol{\alpha}\hat{\boldsymbol{x}} + \boldsymbol{\beta}\boldsymbol{u} + \hat{\boldsymbol{h}} + \boldsymbol{U}_{smo} \\ \dot{\hat{\boldsymbol{h}}} &= \boldsymbol{G}\boldsymbol{U}_{smo} \end{cases} \tag{14}$$

where $\hat{\boldsymbol{x}}$ is the observed value of $\boldsymbol{x}$, $\hat{\boldsymbol{x}} = \left[\hat{i}_d \; \hat{i}_q \; \hat{\omega}_e\right]^T$; $\hat{\boldsymbol{h}}$ is the observed value of $\boldsymbol{h}$, $\hat{\boldsymbol{h}} = \left[\hat{h}_d \; \hat{h}_q \; \hat{h}_\omega\right]^T$; $\boldsymbol{U}_{smo} = \left[U_{dsmo} \; U_{qsmo} \; U_{\omega smo}\right]^T$ is sliding mode control law; $\boldsymbol{G} = diag\left(G_d, G_q, G_\omega\right)$ is parameter matrix.

Subtracting (13) from (14) gives the error dynamics

$$\dot{\boldsymbol{e}}_1 = \boldsymbol{\alpha}\boldsymbol{e}_1 + \boldsymbol{e}_2 - \boldsymbol{U}_{smo} \tag{15}$$

$$\dot{\boldsymbol{e}}_2 = \boldsymbol{H} - \boldsymbol{G}\boldsymbol{U}_{smo} \tag{16}$$

where $\boldsymbol{e}_1 = \left[e_d \; e_q \; e_\omega\right]^T$, $e_d = i_d - \hat{i}_d$, $e_q = i_q - \hat{i}_q$, $e_\omega = \omega_e - \hat{\omega}_e$; $\boldsymbol{e}_2 = \left[e_{hd} \; e_{hq} \; e_{h\omega}\right]^T$, $e_{hd} = h_d - \hat{h}_d$, $e_{hq} = h_q - \hat{h}_q$, and $e_\omega = h_\omega - \hat{h}_\omega$.

Selecting the sliding surface to be $\boldsymbol{s} = \boldsymbol{e}_1$. To improve the observation precision of the ESMO, the exponential reaching law is chosen as

$$\dot{\boldsymbol{s}} = -\boldsymbol{k}sgn(\boldsymbol{s}) - \boldsymbol{\lambda}\boldsymbol{s} \tag{17}$$

where $\boldsymbol{k} = diag(k_1, k_2, k_3)$ and $\boldsymbol{\lambda} = diag(\lambda_1, \lambda_2, \lambda_3)$ are the parameters matrix, both of them are positive.

Then, substituting (17) into (15) yields

$$\boldsymbol{\alpha}\boldsymbol{e}_1 + \boldsymbol{e}_2 - \boldsymbol{U}_{smo} = -\boldsymbol{k}sgn(\boldsymbol{e}) - \boldsymbol{\lambda}\boldsymbol{e}. \tag{18}$$

Theorem 1. *Consider $\boldsymbol{e}_2$ as the disturbances of $\boldsymbol{U}_{smo}$ and design the sliding mode control law*

$$\boldsymbol{U}_{smo} = (\boldsymbol{\alpha} + \boldsymbol{\lambda})\boldsymbol{e}_1 + \boldsymbol{k}sgn(\boldsymbol{e}_1) \tag{19}$$

then, the error equations (15) and (16) are asymptotically stable, and the error $\boldsymbol{e}_1$ converges in finite time.

Proof: Considering a Lyapunov function candidate to be

$$V = \frac{1}{2}\boldsymbol{e}_1^T\boldsymbol{e}_1. \tag{20}$$

Differentiating Lyapunov function (20), and substituting (15) and (19) into yields

$$\begin{aligned} \dot{V} &= \boldsymbol{e}_1^T\dot{\boldsymbol{e}}_1 = \boldsymbol{e}_1^T\left(-\boldsymbol{\lambda}\boldsymbol{e}_1 + \boldsymbol{e}_2 - \boldsymbol{k}sgn(\boldsymbol{e}_1)\right) \\ &\le \boldsymbol{e}_1^T\boldsymbol{e}_2 - k_1\|e_d\| - k_2\|e_q\| - k_3\|e_\omega\| \\ &\le \|\boldsymbol{e}_1\|\|\boldsymbol{e}_2\| - k_4\|\boldsymbol{e}_1\| = \|\boldsymbol{e}_1\|(\|\boldsymbol{e}_2\| - k_4) \end{aligned} \tag{21}$$

where $\|\cdot\|$ is the norm of a vector, $k_4 = \min\{k_1, k_2, k_3\}$.

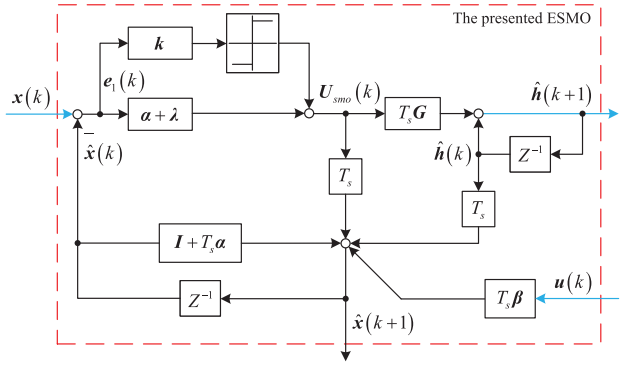

FIGURE 2. Discrete block diagram of the presented ESMO.

In engineering, $\|\boldsymbol{e}_2\|$ in (21) is considered to be bounded, namely, $\|\boldsymbol{e}_2\| \leq \xi$. Thus, if k_4 is chosen to be $k_4 \geq \xi + \eta$ ($\eta > 0$), then

$$\dot{V} \leq -\eta \|\boldsymbol{e}_1\| < 0. \tag{22}$$

holds.

This completes the proof. □

According to the equivalent principle of sliding mode, we get $\dot{\boldsymbol{e}}_1 = \boldsymbol{e}_1 = 0$. Thus, equations (15) and (16) can be simplified as

$$\dot{\boldsymbol{e}}_2 + \boldsymbol{G}\boldsymbol{e}_2 - \boldsymbol{H} = 0. \tag{23}$$

The solution of (23) is $\boldsymbol{e}_2 = e^{-\boldsymbol{G}t}\left[\boldsymbol{C}_1 + \int \boldsymbol{H} \cdot e^{-\boldsymbol{G}t} dt\right]$, where $\boldsymbol{C}_1$ is a constant matrix. It is clear that the parameter matrix $\boldsymbol{G}$ must be positive to ensure the convergence of $\boldsymbol{e}_2$, and the convergence rate is directly related to $\boldsymbol{G}$.

B. DISCRETIZATION OF ESMO

The discrete expression of ESMO (Fig. 2) is expressed as

$$\begin{cases} \hat{\boldsymbol{x}}(k+1) = (\boldsymbol{I} + T_s\boldsymbol{\alpha})\hat{\boldsymbol{x}}(k) + T_s\left(\boldsymbol{\beta}\boldsymbol{u}(k) + \hat{\boldsymbol{h}}(k) + \boldsymbol{U}_{smo}(k)\right) \\ \hat{\boldsymbol{h}}(k+1) = \hat{\boldsymbol{h}}(k) + T_s\boldsymbol{G}\boldsymbol{U}_{smo}(k) \end{cases}$$

where $\hat{\boldsymbol{x}}(k+1) = \left[\hat{i}_d(k+1)\ \hat{i}_q(k+1)\ \hat{\omega}_e(k+1)\right]^T$ is the predictive values at the next sampling time; $\hat{\boldsymbol{h}}(k+1) = \left[\hat{h}_d(k+1)\ \hat{h}_q(k+1)\ \hat{h}_\omega(k+1)\right]^T$ is the predictive values of estimated unknown parts at the next sampling time. $\boldsymbol{U}_{smo}(k)$ satisfies $\boldsymbol{U}_{smo}(k) = (\boldsymbol{\alpha} + \boldsymbol{\lambda})\boldsymbol{e}_1(k) + \boldsymbol{k}sgn(\boldsymbol{e}_1(k))$, where $\boldsymbol{e}_1(k) = \boldsymbol{x}(k) - \hat{\boldsymbol{x}}(k)$.

Remark 3. *The sampling time T_s of the discrete ESMO in the current loops is T_{sc}, and the sampling time T_s of the discrete ESMO in the speed loop is T_{ss}.*

V. SIMULATION ANALYSIS

This section analyzes the performance of the presented MFFTPC method for the SPMSM drive system using MATLAB/Simulink, which is compared with the conventional PI-MPC. The PI-MPC is termed by combining the conventional FCS-MPC control in the current loop with the PI control in the speed loop.

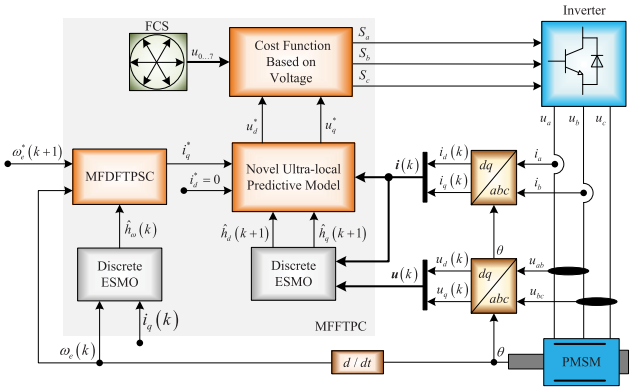

FIGURE 3. Block diagram of MFFTPC for PMSM drive.

TABLE 1. Nominal parameters of SPMSM.

Parameters	Values
Rated power	125 kW
Rated speed	2000 r/min
DC voltage(U_{dc})	1200 V
Stator resistance(R_{so})	0.02 Ω
Number of pole pairs (n_p)	4
Stator inductance(L_{so})	1 mH
Flux linkage PM(ψ_{ro})	0.892 Wb
Rotational Inertia(J)	1.57 kg · m^2
Viscous friction coefficient(B)	0.001 Nm · s/rad

TABLE 2. Performance comparison with load torque changes.

Performance Metrics		PI-MPC	MFFTPC
Settling Time (ms)	q-axis current	5.5	3.5
	torque	5.5	3.5
	speed	85	81
Overshoot (%)	q-axis current	53.8	26.9
	torque	57.1	21.4
	speed	0.4	0
Steady-State Tracking Error	q-axis current (A)	±20	±20
	speed (rad/s)	2	0

The $i_d^* = 0$ control strategy is selected in the PMSM drive system(Fig. 3). The nominal parameters of SPMSM were listed in Table 1. The sampling time of current loops, T_{sc}, was set as 50 μs and the sampling time of speed loop, T_{ss}, was set as 1.5 ms. The parameters of the novel ULM were chosen to be $\alpha_d = \alpha_q = -20$, $\beta_d = \beta_q = 1000$, $\alpha_\omega = 13.6$, and $\beta_\omega = 6.4 \times 10^{-4}$. According to Theorem 1, the parameters of ESMO were chosen to be $k_1 = k_2 = 8 \times 10^5$, $\lambda_1 = \lambda_2 = 1 \times 10^5$, $G_d = G_q = 1 \times 10^4$, $k_4 = 9 \times 10^5$, $\lambda_3 = 1.8 \times 10^5$, and $G_\omega = 9 \times 10^5$.

A. SIMULATION RESULTS FOR SPMSM AT NO-LOAD AND LOAD

The load torque was set to 0 $N \cdot m$ and increased to 700 $N \cdot m$ at 0.2 s. The parameters of the motor were nominal values.

Figs. 4 and 5 show that PI-MPC has a lower speed response than MFFTPC. When the load torque changed to 700 $N \cdot m$ at 0.2 s, the q-axis current and torque controlled by MFFTPC quickly tracked the reference value, but those controlled by PI-MPC had overshoots.

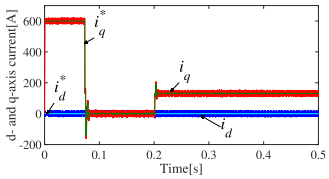

(a) i_d and i_q

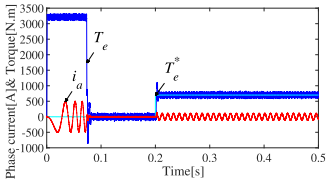

(b) i_a, T_e, and T_e^*

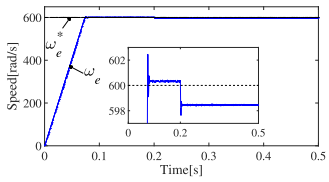

(c) ω_e^* and ω_e

FIGURE 4. Simulation results of conventional PI-MPC with no-load and load.

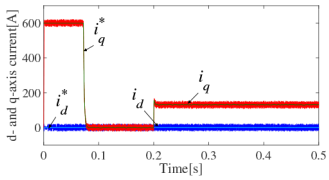

(a) i_d and i_q

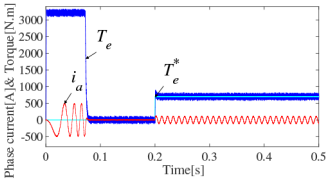

(b) i_a, T_e, and T_e^*

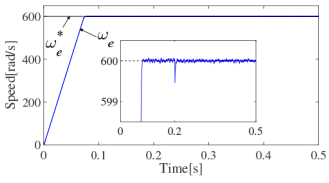

(c) ω_e^* and ω_e

FIGURE 5. Simulation results of MFFTPC with no-load and load.

Table 2 summarized the setting time, overshoot, and steady-state tracking error of the PI-MPC, MFFTPC. The results confirm that the tracking accuracy of the presented MFFTPC was better than that of the PI-MPC.

The unknown parts $\boldsymbol{h}$ in the novel ULM are observed by the sliding mode observer (SMO) and the ESMO for SPMSM with no-load and load. Fig. 6 demonstrates the observation results of the two methods. It shows that the conventional SMO has the chattering due to its own characteristics.

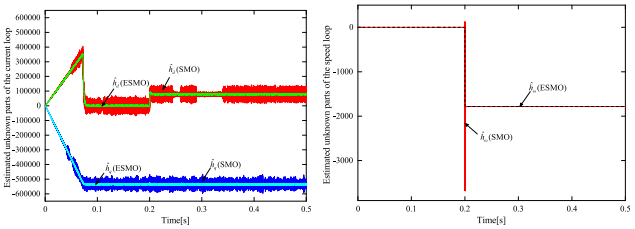

(a) $\hat{h}_\omega$ (b) $\hat{h}_d$ and $\hat{h}_q$

FIGURE 6. Estimated unknown parts with no-load and load.

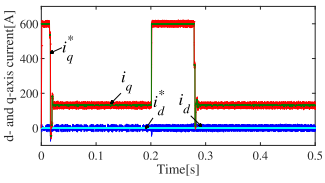

(a) i_d and i_q

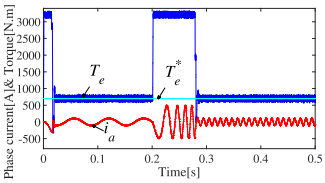

(b) i_a, T_e, and T_e^*

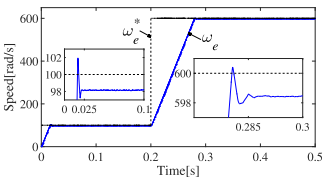

(c) ω_e^* and ω_e

FIGURE 7. Simulation results of conventional PI-MPC at low-speed and high-speed.

However, the unknown part observed by ESMO is more accurate and the chattering is smaller.

B. SIMULATION RESULTS FOR SPMSM AT LOW-SPEED AND HIGH-SPEED

The load torque was set to 700 N·m. The initial reference speed was set to 100 rad/s and increased to 600 rad/s at 0.2 s. The parameters of the motor were nominal values.

Figs. 7 and 8 show that the setting time, overshoot, and steady-state tracking error of the MFFTPC method at low-speed and high-speed were much shorter than those of the conventional PI-MPC. Table 3 listed the setting time, overshoot, and steady-state tracking error. The results confirm that the tracking accuracy of the presented MFFTPC was better than that of the PI-MPC at low-speed and high-speed.

Fig. 9 indicates the unknown parts $\boldsymbol{h}$ in the novel ULM are observed by the SMO and the ESMO for SPMSM at low-speed and high-speed. The results prove that the ESMO has a faster convergence speed and smaller chattering compared to the SMO at both low-speed and high-speed.

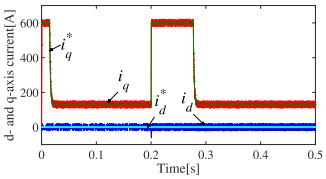

(a) i_d and i_q

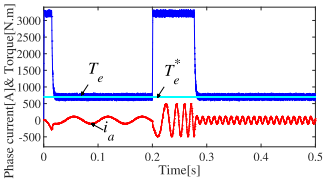

(b) i_a, T_e, and T_e^*

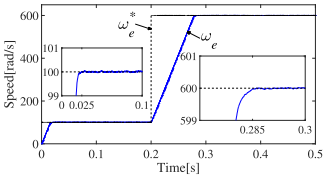

(c) ω_e^* and ω_e

FIGURE 8. Simulation results of MFFTPC at low-speed and high-speed.

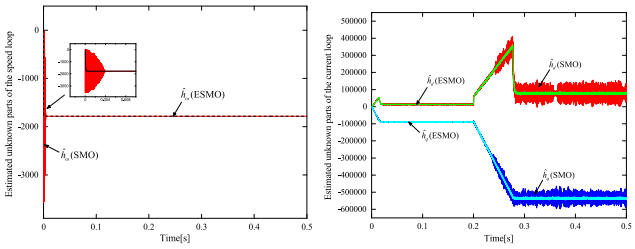

(a) $\hat{h}_\omega$ (b) $\hat{h}_d$ and $\hat{h}_q$

FIGURE 9. Estimated unknown parts at low-speed and high-speed.

TABLE 3. Performance comparison at low and high speed.

	Performance Metrics	PI-MPC	MFFTPC
Low-speed	Settling Time (ms)	24	22
	Overshoot (%)	4.1	0
	Steady-State Tracking Error (rad/s)	1.9	0.04
High-speed	Settling Time (ms)	86	83
	Overshoot (%)	0.33	0
	Steady-State Tracking Error (rad/s)	1.5	0.05

C. SIMULATION RESULTS FOR SPMSM WITH PARAMETER PERTURBATIONS

In this scenario, R_s changed from 0.02 Ω to 0.04 Ω and L_s changed from 1 mH to 2 mH, and other motor parameters were the same as those in subsection V-A.

Figs. 10 and 11 show that the d-q-axis current had deviations, the speed response had overshoot when the resistance and inductance were changed in the PI-MPC control method. However, the the currents and speed response of the MFFTPC method had not similar changes and were consistent with normal conditions. When the load torque changed to 700 $N \cdot m$ at 0.2 s, the current and torque controlled by MFFTPC had overshoot, but they were less than those controlled by PI-MPC, the speed controlled by MFFTPC dropped less than that of PI-MPC.

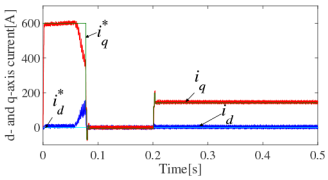

(a) i_d and i_q

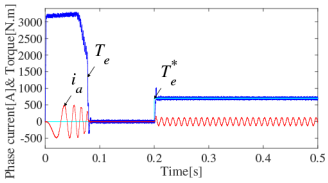

(b) i_a, T_e, and T_e^*

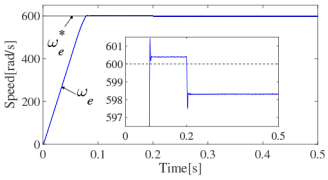

(c) ω_e^* and ω_e

FIGURE 10. Simulation results of conventional PI-MPC with variations of resistance and inductance.

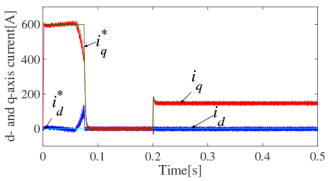

(a) i_d and i_q

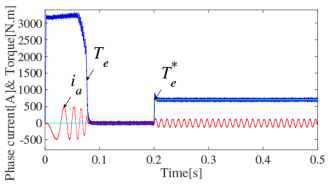

(b) i_a, T_e, and T_e^*

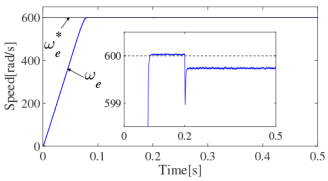

(c) ω_e^* and ω_e

FIGURE 11. Simulation results of MFFTPC with variations of resistance and inductance.

Table 4 summarized the setting time, overshoot, and steady-state tracking error of the MFFTPC and PI-MPC methods when the resistance and inductance were changed. The results confirm that the presented MFFTPC had better performance in the case of parameter perturbations.

Fig. 12 demonstrates the unknown parts $\boldsymbol{h}$ in the novel ULM are observed by the SMO and the ESMO for SPMSM with parameter perturbations. It shows that the conventional

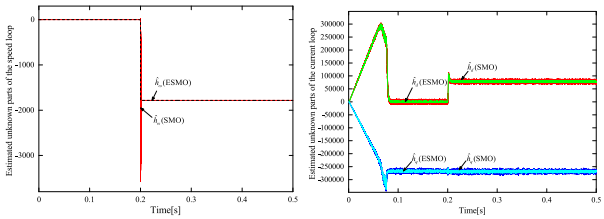

(a) $\hat{h}_\omega$ (b) $\hat{h}_d$ and $\hat{h}_q$

FIGURE 12. Estimated unknown parts with variations of resistance and inductance.

TABLE 4. Performance comparison with variations of resistance and inductance.

Performance Metrics		PI-MPC	MFFTPC
Settling Time (ms)	q-axis current	4.5	3.1
	torque	4.5	3.1
	speed	86	82
Overshoot (%)	q-axis current	44.8	24.1
	torque	42.9	27.1
	speed	0.25	0
Steady-State Tracking Error	d-axis current (A)	+15, -10	±15
	q-axis current (A)	+15, -8	±10
	speed (rad/s)	2.5	0.3

SMO has the chattering and the ESMO has smaller chattering. When parameter perturbations occur, the observed values of the unknown parts $\boldsymbol{h}$ change accordingly, and accurate estimation of the unknown part $\boldsymbol{h}$ can update the predictive model to match the actual model. This is also the reason why parameter perturbations have a relatively small impact on MFFTPC.

D. SIMULATION RESULTS FOR SPMSM WITH DEMAGNETIZATION

The simulation conditions were the same as those in subsection V-A. The initial amplitude ψ_{ro} and deviation angle γ of the PM were 0.892 Wb and 0°, ψ_r changed to 0.446 Wb at 0.3 s, and the deviation angle γ changed to 45° at 0.4 s.

Figs. 13 and 14 show that when the PM flux amplitude decreased at 0.3 s, the recovering time of torque controlled by PI-MPC was longer than that of the MFFTPC, and the speed controlled by PI-MPC was reduced. When the deviation angle γ is set to 45° at 0.4 s, the recovering time of torque controlled by MFFTPC is shorter than that of the PI-MPC, and the speed controlled by PI-MPC was further reduced. However, the MFFTPC had not similar changes.

Table 5 summarized the results of the steady-state tracking error of current and speed, and recovering time of toque by PI-MPC and MFFTPC methods. The simulation results verify the presented method suppresses the influence of demagnetization fault and performs the fault-tolerant control.

Fig. 15 demonstrates the unknown parts $\boldsymbol{h}$ in the novel ULM are observed by the SMO and the ESMO for SPMSM with demagnetization. When PM demagnetization fault occurs, the ESMO can adjust accordingly by estimating the unknown part $\boldsymbol{h}$, which is more accurate in real-time updating the predictive model for MFFTPC compared to the SMO.

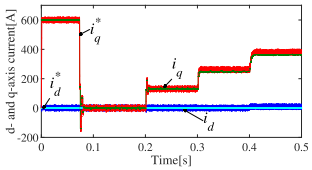

(a) i_d and i_q

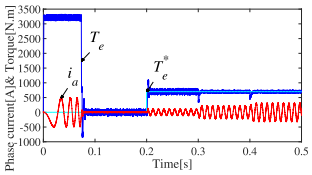

(b) i_a, T_e, and T_e^*

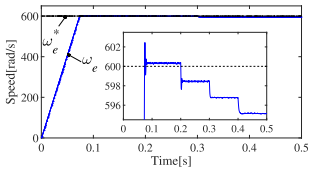

(c) ω_e^* and ω_e

FIGURE 13. Simulation results of conventional PI-MPC with PM demagnetization fault.

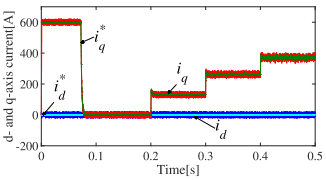

(a) i_d and i_q

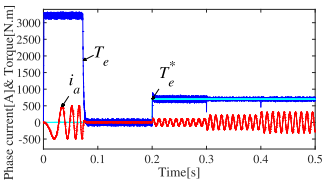

(b) i_a, T_e, and T_e^*

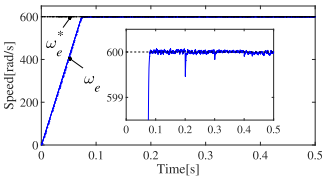

(c) ω_e^* and ω_e

FIGURE 14. Simulation results of MFFTPC with PM demagnetization fault.

VI. EXPERIMENTAL VERIFICATION

This section presents a hardware-in-the-loop simulation (HILS) experiment to validate the presented MFFTPC method. The RT-LAB OP5600 is implemented the HILS experiment of the PMSM drive system (Fig. 16). Fig. 16(b) shows the configuration of HILS. The TMS320F2812 DSP is the controller, and the RT-LAB OP5600 is constructed as the PMSM and inverter, etc. The system parameters are consistent with the simulation parameters.

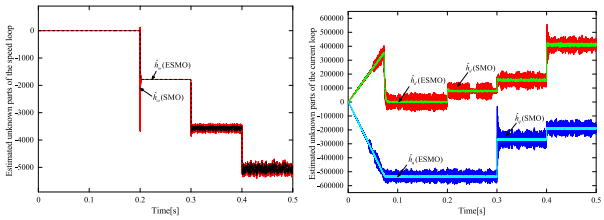

(a) $\hat{h}_\omega$ (b) $\hat{h}_d$ and $\hat{h}_q$

FIGURE 15. Estimated unknown parts with PM demagnetization fault.

TABLE 5. Performance comparison with PM demagnetization fault.

Performance Metrics			PI-MPC	MFFTPC
The Amplitude of PM Changed	Steady-State Tracking Error	d-axis current (A)	±20	±20
		q-axis current (A)	+31, -9	±20
		speed	3.2	0.04
	Recovering Time of Torque (ms)		3.1	0.4
The Deviation Angle of PM Changed	Steady-State Tracking Error	d-axis current (A)	+30, -10	±20
		q-axis current (A)	+38, -2	±20
		speed	4.9	0.06
	Recovering Time of Torque (ms)		5.1	0.4

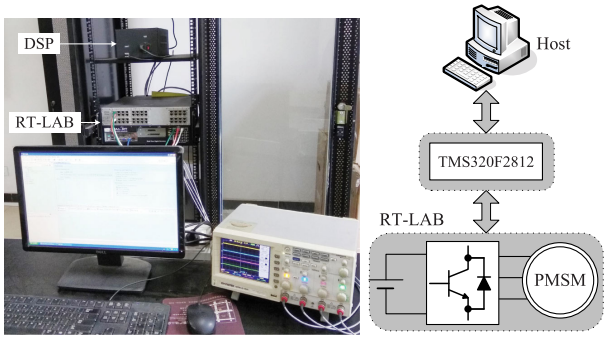

(a) Platform (b) Configuration of HILS

FIGURE 16. RT-LAB HILS.

A. EXPERIMENTAL RESULTS FOR SPMSM IN NORMAL CONDITION

The experimental conditions were the same as those in subsection V-A. Similar to the simulation, the load torque is given a step reference in the steady-state process. Fig. 17 shows that after the load torque changed, the variation of the q-axis current and torque controlled by MFFTPC were small and can be ignored, but those are larger when using the PI-MPC. The speed deviation also exist in PI-MPC when load torque changed. It can be seen that the MFFTPC method is obviously better than the conventional PI-MPC in normal condition.

B. EXPERIMENTAL RESULTS FOR SPMSM WITH PARAMETER VARIATIONS

The experimental conditions were the same as those in subsection V-C. Fig. 18 shows a comparison of the presented MFFTPC and the conventional PI-MPC with parameter variations. The current, torque and speed using the PI-MPC have deviation and overshoot (Fig. 18(a)). By contrast, the MFFTPC method has same performance as it in normal condition (Fig. 18(b)). Fig. 18 shows that the presented MFFTPC exhibits the robustness to the parameter variations.

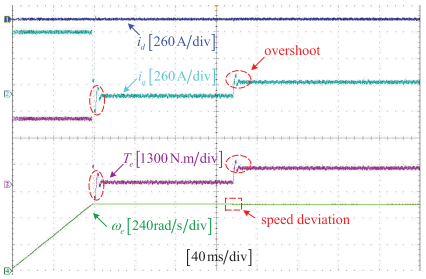

(a) PI-MPC

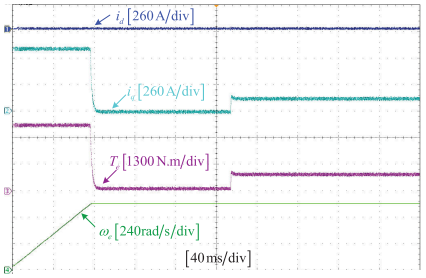

(b) MFFTPC

FIGURE 17. Experimental results of the d- and q-axes current, torque, and speed with normal condition.

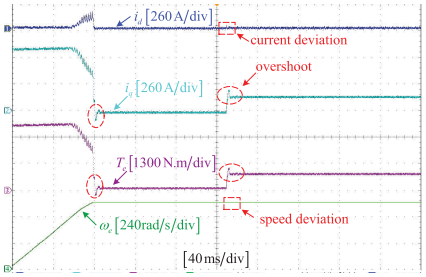

(a) PI-MPC

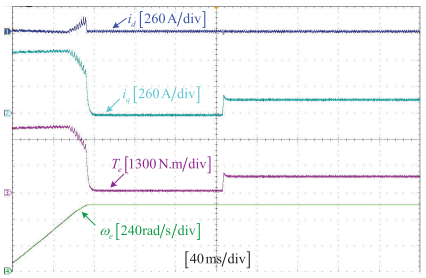

(b) MFFTPC

FIGURE 18. Experimental results of the d- and q-axes current, torque, and speed with parameter variations.

C. EXPERIMENTAL RESULTS FOR SPMSM WITH PM DEMAGNETIZATION FAULT

The experimental conditions were the same as those in subsection V-D. Fig. 19 shows a comparison of the MFFTPC and the PI-MPC method with PM demagnetization fault. It is obvious that the variations of the PM amplitude and the deviation angle exert an effect on torque responses in the conventional PI-MPC method (Fig. 19(a)). The recovering time of torque using the PI-MPC are obviously larger; by contrast, the torque recovered smoothly by MFFTPC method (Fig. 19(b)). In addition, it can be known from

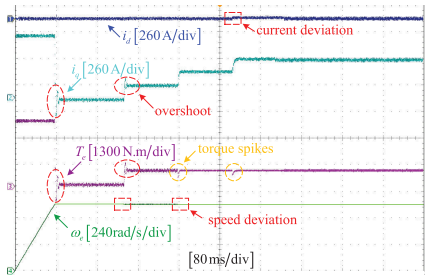

(a) PI-MPC

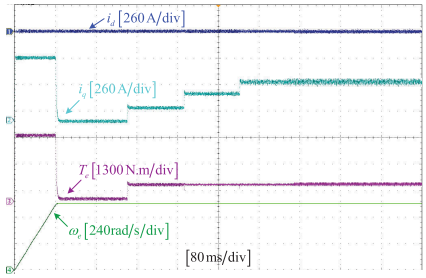

(b) MFFTPC

FIGURE 19. Experimental results of the *d*- and *q*-axes current, torque, and speed with PM demagnetization fault.

Fig. 19 that PI-MPC has the current and speed deviation when PM demagnetization fault occurred. Thus, compared with the conventional PI-MPC, the proposed MFFTPC has significantly improved fault-tolerance capability of PM demagnetization faults.

VII. CONCLUSION

This paper presented an MFFTPC approach to eliminate the effects of parameter mismatches caused by motor parameter perturbations. First, we proposed a novel ULM of the current loop and speed loops considering the parameter perturbations for an SPMSM drive system. Next, we presented the ESMO-based MFFTPC approach. We designed an FCS-MFFTPCC in the current loops and a MFDFTPSC in the speed loop based on the novel ULM. We presented the voltage-based cost function to obtain the optimal voltage vector, which is calculated and compared only once. Then, we designed the discrete ESMO to timely obtain information about the unknown part of the novel ULM. It can compensate for the parameter mismatch error caused by the parameter perturbation of the conventional MPC.

The simulation and experimental results show that the presented method has better transient, steady-state performance, and stronger robustness. The presented method effectively maintained the control performance and reduced the dependence on the accurate model of SPMSM.

REFERENCES

[1] H. Wang, W. Sun, D. Jiang, and R. Qu, "A MTPA and flux-weakening curve identification method based on physics-informed network without calibration," *IEEE Trans. Power Electron.*, vol. 38, no. 10, pp. 12370–12375, Oct. 2023.

[2] K. Zhao, R. Zhou, J. She, C. Zhang, J. He, G. Huang, and X. Li, "Demagnetization-fault reconstruction and tolerant-control for PMSM using improved SMO-based equivalent-input-disturbance approach," *IEEE/ASME Trans. Mechatronics*, vol. 27, no. 2, pp. 701–712, Apr. 2022.

[3] S. Liu, C. Liu, H. Zhao, Y. Liu, and Z. Dong, "Improved flux weakening control strategy for five-phase PMSM considering harmonic voltage vectors," *IEEE Trans. Power Electron.*, vol. 37, no. 9, pp. 10967–10980, Sep. 2022.

[4] M. F. Elmorshedy, W. Xu, F. F. M. El-Sousy, M. R. Islam, and A. A. Ahmed, "Recent achievements in model predictive control techniques for industrial motor: A comprehensive state-of-the-art," *IEEE Access*, vol. 9, pp. 58170–58191, 2021.

[5] J. Chen, Y. Qin, A. M. Bozorgi, and M. Farasat, "Low complexity dual-vector model predictive current control for surface-mounted permanent magnet synchronous motor drives," *IEEE J. Emerg. Sel. Topics Power Electron.*, vol. 8, no. 3, pp. 2655–2663, Sep. 2020.

[6] P. Karamanakos and T. Geyer, "Guidelines for the design of finite control set model predictive controllers," *IEEE Trans. Power Electron.*, vol. 35, no. 7, pp. 7434–7450, Jul. 2020.

[7] F. Wang, L. He, and J. Rodríguez, "A robust predictive speed control for SPMSM systems using a sliding mode gradient descent disturbance observer," *IEEE Trans. Energy Convers.*, vol. 38, no. 1, pp. 540–549, Mar. 2023.

[8] C. Sain, A. Banerjee, and P. K. Biswas, "Modelling and comparative dynamic analysis due to demagnetization of a torque controlled permanent magnet synchronous motor drive for energy-efficient electric vehicle," *ISA Trans.*, vol. 97, pp. 384–400, Feb. 2020.

[9] K. Zhao, A. Leng, R. Zhou, W. Dai, S. Wu, and T. Li, "Demagnetization fault reconstruction for six-phase permanent magnet synchronous motor by improved super-twisting algorithm-based sliding-mode observer," *Measurement*, vol. 172, Feb. 2021, Art. no. 108905.

[10] S. Li, Y. Xu, W. Zhang, and J. Zou, "Robust deadbeat predictive direct speed control for PMSM with dual second-order sliding-mode disturbance observers and sensitivity analysis," *IEEE Trans. Power Electron.*, vol. 38, no. 7, pp. 8310–8326, Jul. 2023.

[11] L. Verkroost, J. Druant, H. Vansompel, F. De Belie, and P. Sergeant, "Performance degradation of surface PMSMs with demagnetization defect under predictive current control," *Energies*, vol. 12, no. 5, p. 782, Feb. 2019.

[12] C. Lian, F. Xiao, J. Liu, and S. Gao, "Parameter and VSI nonlinearity hybrid estimation for PMSM drives based on recursive least square," *IEEE Trans. Transport. Electrific.*, vol. 9, no. 2, pp. 2195–2206, Sep. 2023.

[13] T. B. D. Santos, I. Oliani, R. Figueiredo, D. Albieiro, A. Pelizari, and A. J. S. Filho, "Robust finite control set model predictive current control for induction motor using deadbeat approach in stationary frame," *IEEE Access*, vol. 11, pp. 13067–13078, 2023.

[14] T. Tao, W. Zhao, Y. Du, Y. Cheng, and J. Zhu, "Simplified fault-tolerant model predictive control for a five-phase permanent-magnet motor with reduced computation burden," *IEEE Trans. Power Electron.*, vol. 35, no. 4, pp. 3850–3858, Apr. 2020.

[15] P. G. Carlet, A. Favato, S. Bolognani, and F. Dörfler, "Data-driven continuous-set predictive current control for synchronous motor drives," *IEEE Trans. Power Electron.*, vol. 37, no. 6, pp. 6637–6646, Jun. 2022.

[16] X. Zhang and Z. Wang, "Simple robust model predictive current control for PMSM drives without flux-linkage parameter," *IEEE Trans. Ind. Electron.*, vol. 70, no. 4, pp. 3515–3524, Apr. 2023.

[17] Y. Yao, Y. Huang, F. Peng, J. Dong, and H. Zhang, "An improved deadbeat predictive current control with online parameter identification for surface-mounted PMSMs," *IEEE Trans. Ind. Electron.*, vol. 67, no. 12, pp. 10145–10155, Dec. 2020.

[18] F. Mahmouditabar, A. Vahedi, and F. Marignetti, "The demagnetization phenomenon in PM machines: Principles, modeling, and design considerations," *IEEE Access*, vol. 11, pp. 47750–47773, 2023.

[19] Y. Zhang and T. Jiang, "Robust predictive stator current control based on prediction error compensation for a doubly fed induction generator under nonideal grids," *IEEE Trans. Ind. Electron.*, vol. 69, no. 5, pp. 4398–4408, May 2022.

[20] I.-H. Kao, W.-J. Wang, Y.-H. Lai, and J.-W. Perng, "Analysis of permanent magnet synchronous motor fault diagnosis based on learning," *IEEE Trans. Instrum. Meas.*, vol. 68, no. 2, pp. 310–324, Feb. 2019.

[21] J. Xie, Z. Long, X. Zhang, G. Qin, F. Huang, and Z. Rao, "Demagnetization fault diagnosis of PMSM using custom phase space reconstruction image," *IEEE Trans. Instrum. Meas.*, vol. 72, pp. 1–11, 2023.

[22] M. Zhu, B. Yang, W. Hu, G. Feng, and N. C. Kar, "Vold–Kalman filtering order tracking based rotor demagnetization detection in PMSM," *IEEE Trans. Ind. Appl.*, vol. 55, no. 6, pp. 5768–5778, Nov. 2019.

[23] W. Hu, T. Wang, and F. Chu, "Novel Ramanujan digital twin for motor periodic fault monitoring and detection," *IEEE Trans. Ind. Informat.*, vol. 19, no. 12, pp. 11564–11572, Dec. 2023.
[24] Y. Han, S. Chen, C. Gong, X. Zhao, F. Zhang, and Y. Li, "Accurate SM disturbance observer-based demagnetization fault diagnosis with parameter mismatch impacts eliminated for IPM motors," *IEEE Trans. Power Electron.*, vol. 38, no. 5, pp. 5706–5710, May 2023.
[25] M. Fliess and C. Join, "Model-free control," *Int. J. Control*, vol. 86, no. 12, pp. 2228–2252, Jul. 2013.
[26] K. Zhao, T. Yin, C. Zhang, J. He, X. Li, Y. Chen, R. Zhou, and A. Leng, "Robust model-free nonsingular terminal sliding mode control for PMSM demagnetization fault," *IEEE Access*, vol. 7, pp. 15737–15748, 2019.
[27] K. Zhao, N. Jia, J. She, W. Dai, R. Zhou, W. Liu, and X. Li, "Robust model-free super-twisting sliding-mode control method based on extended sliding-mode disturbance observer for PMSM drive system," *Control Eng. Pract.*, vol. 139, Oct. 2023, Art. no. 105657.
[28] Y. Zhao, X. Liu, H. Yu, and J. Yu, "Model-free adaptive discrete-time integral terminal sliding mode control for PMSM drive system with disturbance observer," *IET Electr. Power Appl.*, vol. 14, no. 10, pp. 1756–1765, Oct. 2020.
[29] Y. Zhou, H. Li, and H. Zhang, "Model-free deadbeat predictive current control of a surface-mounted permanent magnet synchronous motor drive system," *J. Power Electron.*, vol. 18, no. 1, pp. 103–115, Jan. 2018.
[30] X. Xiao, C. Chen, and M. Zhang, "Dynamic permanent magnet flux estimation of permanent magnet synchronous machines," *IEEE Trans. Appl. Supercond.*, vol. 20, no. 3, pp. 1085–1088, Jun. 2010.
[31] G. Wu, S. Huang, Q. Wu, C. Zhang, F. Rong, and Y. Hu, "Predictive torque and stator flux control for N*3-phase PMSM drives with parameter robustness improvement," *IEEE Trans. Power Electron.*, vol. 36, no. 2, pp. 1970–1983, Feb. 2021.
[32] A. Safaei and M. N. Mahyuddin, "Adaptive model-free control based on an ultra-local model with model-free parameter estimations for a generic SISO system," *IEEE Access*, vol. 6, pp. 4266–4275, 2018.
[33] Y. Zhang, T. Jiang, and J. Jiao, "Model-free predictive current control of DFIG based on an extended state observer under unbalanced and distorted grid," *IEEE Trans. Power Electron.*, vol. 35, no. 8, pp. 8130–8139, Aug. 2020.
[34] J. Gao, C. Gong, W. Li, and J. Liu, "Novel compensation strategy for calculation delay of finite control set model predictive current control in PMSM," *IEEE Trans. Ind. Electron.*, vol. 67, no. 7, pp. 5816–5819, Jul. 2020.

SHU CHENG received the B.E. degree in automation from the East China University of Science and Technology, Shanghai, China, in 2003, and the M.S. and Ph.D. degrees in electrical engineering from Central South University (CSU), Changsha, China, in 2006 and 2011, respectively.

He is a Professor with the School of Traffic and Transportation Engineering, CSU. His research interests include fault diagnosis, fault-tolerant control of electrical drivers, and electric traction control technology.

RUIRUI ZHOU (Graduate Student Member, IEEE) received the B.S. degree from the Heilongjiang University of Science and Technology, Harbin, China, in 2018, and the M.S. degree from the Hunan University of Technology, Zhuzhou, China, in 2021, both in electrical engineering. He is currently pursuing the Ph.D. degree in traffic information engineering and control with Central South University, Changsha, China.

His research interests include predictive control, fault diagnosis for power electronics, and motor drives.

ZHUOXIN LI received the B.S. degree in traffic equipment and control engineering from Central South University, Changsha, China, in 2019, where he is currently pursuing the Ph.D. degree in traffic and transportation engineering.

His research interests include predictive control, fault diagnosis for power electronics, and motor drives.

ZHEN XI received the B.S. degree in mechanical engineering from the Qingdao University of Science and Technology, Qingdao, China, in 2020. He is currently pursuing the M.S. degree in transportation engineering with Central South University, Changsha, China.

His research interests include battery fault diagnosis and state detection.

JUNDONG ZHAO received the M.S. degree in transportation engineering from Central South University, Changsha, China, in 2019, where he is currently pursuing the Ph.D. degree in transportation engineering.

His research interests include control techniques and fault diagnosis of power electronic converters.

KAIHUI ZHAO (Senior Member, IEEE) received the B.S. degree in engineering from Central South University (CSU), Changsha, China, in 1997, the M.S. degree in engineering from Southeast University, Nanjing, China, in 2005, and the Ph.D. degree in engineering from CSU, in 2015.

He was a Japan Society for the Promotion of Science (JSPS) Postdoctoral Fellow with the Tokyo University of Technology, from 2019 to 2021. In 2005, he joined the School of Electrical and Information Engineering, Hunan University of Technology, Zhuzhou, China, where he is currently a Professor. His research interests include fault diagnosis on electric machines and industrial process control.

CHAOQUN XIANG (Member, IEEE) received the B.E. degree in automation, the M.S. degree in electrical engineering, and the Ph.D. degree in transportation engineering from Central South University (CSU), Changsha, China, in 2010, 2013, and 2018, respectively.

His research interests include multilevel converters technology, electric traction control technology, and fault tolerant control of power electronic converters.